fluids

MDPI

Article

Numerical Investigation of Noise Generation from a Variable-Pitch Propeller at Various Flight Conditions

Mateus Grassano Lattari [1,*], Victor Henrique Pereira da Rosa [1], Filipe Dutra da Silva [2] and César José Deschamps [1]

[1] Departamento de Engenharia Mecânica, Universidade Federal de Santa Catarina—UFSC, Campus Universitário, Bairro Trindade, Florianópolis 88040-900, SC, Brazil; vhprosa@me.com (V.H.P.d.R.); deschamps@polo.ufsc.br (C.J.D.)

[2] Departamento de Engenharia Mecânica, Universidade Federal de Santa Catarina—UFSC, Campus Universitário, Block U, Industrial District, Joinville 89219-600, SC, Brazil; filipe.dutra@teg.ufsc.br

* Correspondence: mateus.grassano@polo.ufsc.br

Abstract

The advent of electric propulsion for new aircraft designs necessitates the optimization of propeller aerodynamic performance and the reduction of acoustic signatures. Variable-pitch propellers present a promising solution, offering the flexibility to adjust blade angles in response to different flight conditions. The study investigates the performance of blade pitch configurations tailored to specific flight conditions. Rather than a dynamic pitch change, the research evaluates discrete pitch settings coupled with corresponding advance ratios to identify optimal operating points. Findings show that increasing collective pitch in response to a higher advance ratio (forward flight) successfully maintains aerodynamic efficiency and thrust, with an expected increase in torque. While this adjustment leads to an anticipated rise in noise due to higher aerodynamic loading, results reveal that a collective pitch increment of $+5^{\circ}$ actively suppresses broadband noise at frequencies above 2 kHz. Analysis of the flow field and surface pressure fluctuations indicates this suppression is directly attributed to the mitigation of outboard propeller stall. Ultimately, this work demonstrates the feasibility of using collective pitch adjustments not only to enhance flight performance but also to actively control and suppress components of the propeller noise signature, such as the broadband noise.

Keywords: VLES; collective pitch angle; broadband noise

Check for updates

Academic Editor: Tian Li

Received: 12 December 2025
Revised: 15 January 2026
Accepted: 21 January 2026
Published: 26 January 2026

Copyright: © 2026 by the authors. Licensee MDPI, Basel, Switzerland. This article is an open access article distributed under the terms and conditions of the Creative Commons Attribution (CC BY) license.

1. Introduction

Advancements in battery energy density have enabled the design of electric aircraft as a viable alternative to conventional platforms. Electric motors offer distinct advantages over combustion engines, including fewer moving parts, smaller space requirements, and the ability to deliver high instantaneous torque across a wide range of shaft speeds [1]. This high-torque capability eliminates the need for reduction gearboxes often required by combustion engines, enabling flexible propeller operation, such as varying the blade pitch angle. The primary challenge remains the low energy density of batteries compared to fossil fuels. As reported by Rohacs and Rohacs [2], the conceptual electrification of a Cessna-172 resulted in a threefold increase in mass and a limited flight range, confining these aircraft to short-range missions.

The limited range of electric aircraft makes them ideal candidates for urban air mobility and unmanned local deliveries, operating in close proximity to populated areas

makes community noise a critical design constraint, governed by strict regulations such as "Annex 16" [3]. For these propeller-driven aircraft, noise emissions are a primary concern. Propeller noise originates from two main sources: periodic and non-deterministic [4]. The periodic sources generate distinct tones at multiples of the Blade Passing Frequency (BPF), which dominate the low-frequency spectrum, however non-deterministic sources distribute their energy across a wide range of frequencies, creating broadband noise that becomes the most significant component at higher frequencies.

Varying the blade pitch angle offers a method to reduce noise emissions while maintaining aerodynamic performance in forward flight. According to some of the results of Yang et al. [5], the pitch angle, measured between the airfoil chord and the propeller's plane of rotation, can be adjusted to maintain an optimal angle of attack along the blades, improving take-off, climb, and overall energy efficiency [6]. Most importantly, higher pitch angles can allow a propeller to generate the same thrust at lower rotational speeds, leading to a reduction in noise emissions compared to simply increasing the propeller's rotation. This strategy is particularly well-suited for electric motors, which can provide the required torque to operate variable-pitch or constant-speed propellers, which can be demanding on combustion engines, resulting in inefficiencies.

Experimental studies have demonstrated noise reductions from varying the propeller pitch angle. Measurements have shown that increasing the pitch angle can reduce the overall sound pressure level by up to 6.5 dB [7] and that coupling a variable-pitch propeller with an electric motor can reduce take-off noise by as much as 12 dB(A) [8]. Podsędkowski et al. [9] experimentally evaluated a variable-pitch propeller mounted on a multicopter rotor system and found that changing the blade angle yields a 31% increase in maximum thrust and raises the thrust-to-power coefficient (CTh) by 2.6–7.5% relative to the factory-fixed pitch, while the motor remains efficient above 80% only when the RPM exceeds roughly 2700 rpm.

Recent studies have elucidated critical nuances in pitch effects, an important finding is that even a modest increase in collective pitch to approximately 5° marks a threshold where the broadband noise starts to increase, as stall begins to unfold on the blade. For higher collective pitch increments a much larger portion of the blade is dominated by outerboard stall [10]. Huang et al. [11] also corroborates that low pitch settings generate weak increments in broadband noise, however the study stress that the dynamic between broadband noise and BPF levels is shifted due to collective pitch increments. On the other hand, the benefits of increasing the collective pitch indicate that the light-to-drag ratio regime can be substantially improved; as reported by Liu et al. [12], where an increment to around 8.2° was responsible to improve the light-to-drag ratio from 2.5 to 3.05 kg/kW. Yu et al. [13] observed that torque increases nonlinearly with pitch, and thrust can stall and drop sharply beyond a critical angle. While prior research on variable-pitch propellers has advanced the current understanding of their aerodynamic and acoustic behavior—ranging from full-scale aircraft applications to small-scale propellers—many of the studies simply report experimental findings or validate simulations without investigating the aeroacoustic mechanisms responsible for the effects of pitch variation on noise. In contrast, this research proposes to investigate the tonal and broadband noise effects of varying the propeller pitch through high-fidelity simulations, while carefully validating them against paired experiments.

For accurately reproducing this phenomenon, results can be obtained through physical experiments or through high-fidelity numerical simulations. Experiments have the main advantage of ensuring physical consistency, demonstrating difficulties in terms of acoustic isolation, and controlling flow recirculation. Numerical simulations can suppress some of the difficulties of controlling this complexity, but they rely on the specific physical model, which can not capture the entire flow physics, considering discretization limitations

or necessary physical simplification to achieve computational cost feasibility. The Very Large Eddy Simulation (VLES) in PowerFLOW [14] approach has gained traction, offering accuracy comparable to classical Large Eddy Simulation (LES) at a significantly lower computational cost [15]. VLES has been used to predict the aerodynamic and acoustic characteristics of various propeller configurations with high accuracy [16–18].

This work conducts a parametric study of pitch angle increments in a small-scale and low-Reynolds-number propeller (diameter equivalent to 240 mm $Re < 10^4$), analyzing its aerodynamic performance and noise levels via PowerFLOW's VLES. This research explores the effect of varying the pitch angle across 5, 10, and 15 degrees at rotational speeds of 100, 110, and 120 RPS. Although propellers of this size are commonly designed for drones, the inclusion of a positive advance ratio with zero yaw angle locates this investigation in conditions more common to eVTOL aircraft. The choice of a small-scale propeller makes the simulation more suitable for mimicking experiments, given the size of typical anechoic chambers. The analysis will focus on spectral noise data, thrust, torque, velocity fields, and vortex magnitudes along different blade sections. Pressure time derivative on the propeller surface will be investigated to provide a deeper understanding of the noise generation mechanisms. This paper is divided into methodology, results, and conclusions.

2. Methodology

2.1. Methods

PowerFLOW v2021-R5 executes a VLES hybrid LBM–RNG k–ϵ scheme; turbulent scales resolved by the Cartesian mesh are advanced with the BGK collision operator,

$$f_i(\mathbf{x} + \mathbf{c}_i \triangle t, t + \triangle t) = f_i(\mathbf{x}, t) + C(\mathbf{x}, t), \tag{1}$$

where f is the probability density function and $C(\mathbf{x}, t)$ is the molecular collision term. While sub-grid contributions appear as an effective viscosity whose relaxation time is fixed by the Chapman–Enskog expansion [19]. Default closure coefficients are retained. Turbulent accounting relies on RNG transport equations, defined as

$$\frac{\partial k}{\partial t} + \vec{u} \cdot \nabla k = \nabla \cdot \left[\left(\nu + \frac{\nu_T}{\sigma_k} \right) \nabla k \right] + \frac{P_k}{\rho} - \epsilon, \tag{2}$$

$$\frac{\partial \epsilon}{\partial t} + \vec{u} \cdot \nabla \epsilon = \nabla \cdot \left[\left(\nu + \frac{\nu_T}{\sigma_\epsilon} \right) \nabla \epsilon \right] + C_{\epsilon 1} \frac{\epsilon}{k} \frac{P_k}{\rho} - C_{\epsilon 2} \frac{\epsilon^2}{k}, \tag{3}$$

with $\nu_T = C_\mu k^2 / \epsilon$ and wall functions supply the near-wall momentum flux and σ_k, σ_ϵ, $C_{\epsilon 1}$ and $C_{\epsilon 2}$ are model constants.

Regarding the gas model, 3-D isothermal ideal-gas solver treats compressible unsteady fluctuations. Laminar conditions are imposed on the blade leading edges; transition is triggered by 0.0005 m roughness strips, after which the remainder of the rotor surfaces, hub, pressure and suction sides receive turbulent wall treatment. The transition strip follows the same procedure proposed in Casalino et al. [18], relyng on XFOIL e^N method, integrating linear stability analysis with viscous-inviscid interaction to predict transition strip lines in each airfoil cross-section along the blade span.

A cube mesuring 300 m in length encloses the whole computational domain, having sixteen nested spheres regions halve the cell size at each inward level, delivering 283 cells per characteristic length for the intermediate mesh refine chosen for the results analysis. Cell edge varies from 2.4 m in the far field to 7.3×10^{-5} m at the tips and aeroacoustic source regions, giving 1.05×10^8 voxels. Adaptive time stepping advances the finest scale at $\Delta t = 7.7 \times 10^{-8}$ s. A 5 mm-gap toroidal rotating mesh region embeds the propeller in a rotating reference frame in respect to the remainder of the mesh.

Far-field sound is predicted with the Brès et al. [20] wind-tunnel formulation of the Ffowcs Williams–Hawkings equation. Pressure signature is obtained from a cylindrical measurement involving the propeller. Statistics are gathered over the last 10 of 16 revolutions. Power-spectral densities comply with

$$\mathrm{PSD} = 10\log_{10}\left|\frac{S_{xx}}{(2\times10^{-5})^2}\right|, \tag{4}$$

$$\mathrm{SPL/dB} = \mathrm{PSD} + 10\log_{10}(\Delta f_b), \tag{5}$$

$$\mathrm{OASPL/dB} = 10\log_{10}\Big(\sum_{f=0}^{10\mathrm{kHz}} 10^{\mathrm{SPL}(f)/10}\Big). \tag{6}$$

Finally, aerodynamic loads are calculated by numerically integrating the propeller's surface area and the results are presented using propeller performance coefficients, such as the thrust, torque, and aerodynamic efficiency, which are calculated by

$$C_t = \frac{T}{\rho\, n^2\, D^4} \qquad \text{(thrust coefficient)} \tag{7}$$

$$C_q = \frac{Q}{\rho\, n^2\, D^5} \qquad \text{(torque coefficient)} \tag{8}$$

$$\eta = \frac{C_t\, J}{2\,\pi\, C_q} \qquad \text{(propeller efficiency)} \tag{9}$$

2.2. Parametric Analysis

This study proposed a coupling between the pitch increment (β) and the freestream velocity to parametrically assess collective pitch variations. For that, a dual-bladed 240 mm propeller, based on the model measured by [21], is modified with collective pitch angle increments of its blade, as depicted in Figure 1. The correct coupling between pitch and advance ratio (J = V/nD) will be selected by maintaining a constant aerodynamic efficiency for higher J values.

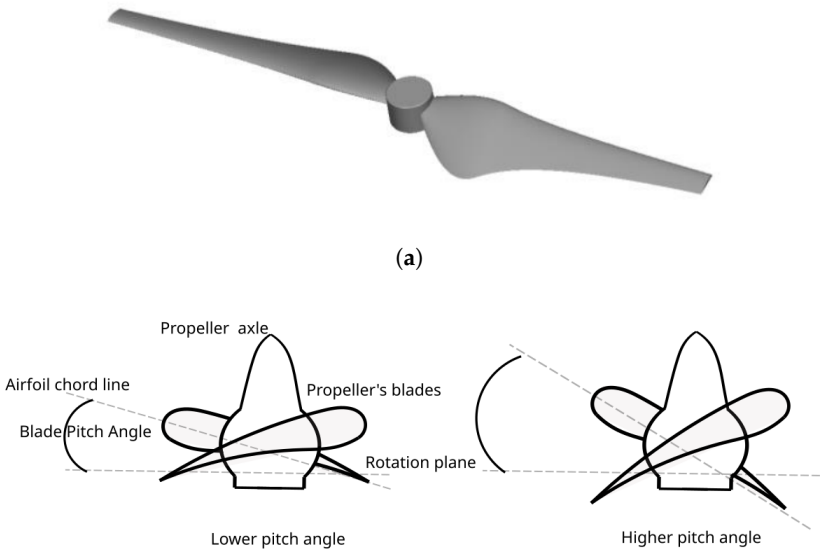


Figure 1. Propeller (**a**) and pitch angle increment definition (**b**).

The blade morphology is defined by a set of spanwise-varying parameters, the distributions of which are illustrated in Figure 2: the radial position r normalized by the

tip radius R_{tip}; the chord distribution c/R_{tip}, which represents the local blade width normalized by the tip radius; the twist angle θ, which defines the local twist angle of the blade section relative to the plane of rotation; the camber distribution dZ_C/R_{tip}, which characterizes the mean-line curvature of the blade profile (dZ_C being the camber height); and the sweep angle, which quantifies the tangential displacement of the blade sections along the span. Finally, the propeller is constructed using a Clark Y airfoil profile.

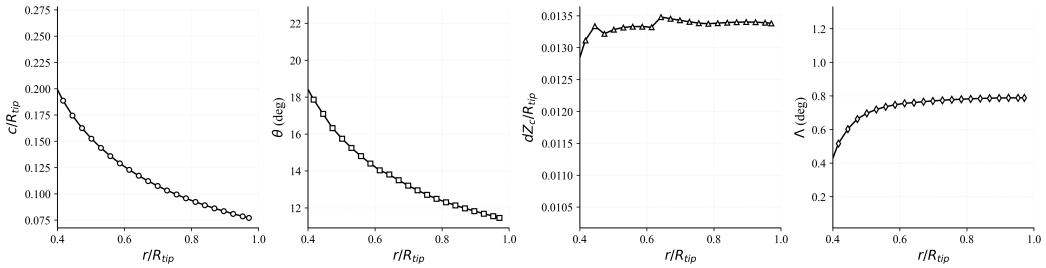


Figure 2. Propeller geometric distribution.

The noise levels are evaluated in selected microphone positions, which are based on the experiments of [21], as depicted in Figure 3.

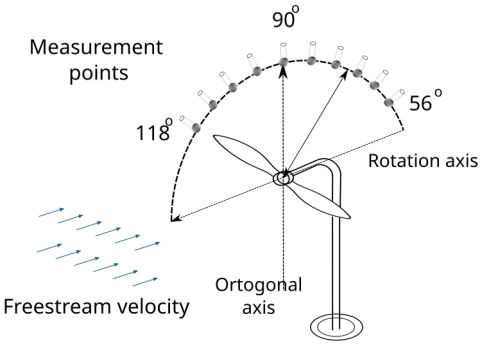


Figure 3. Microphone positions.

3. Results

3.1. Mesh Sensitivity

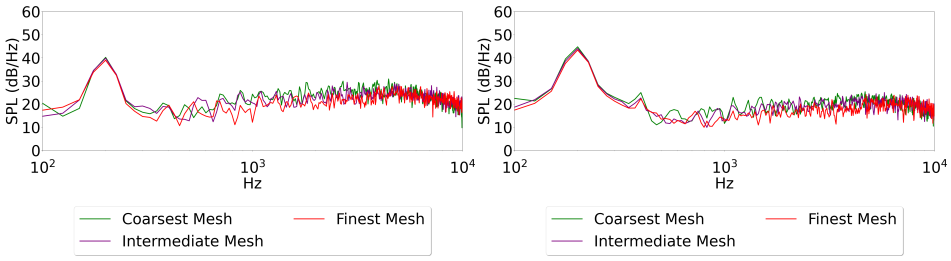
In order to ensure that the mesh provides results with controlled variations with respect to refinement, a sensitivity test is proposed. The coarsest mesh level presents one-half of the cells of the intermediate refinement, and for the finest mesh, those cells are doubled. In Table 1, the thrust and torque coefficients for all refinements, along with their relative errors with respect to the finest mesh, are presented. The results demonstrate that the error is reduced fourfold once the mesh is refined, demonstrating that the intermediate refinement is sufficient for subsequent analyses.

Table 1. Thrust and torque coefficients for mesh refinement.

Mesh	C_T	C_Q	Rel. Error C_T (%)	Rel. Error C_Q (%)
Coarsest	2.43×10^{-2}	1.99×10^{-3}	−7.16	−4.65
Intermediate	2.56×10^{-2}	2.06×10^{-3}	−2.29	−1.15
Finest	2.62×10^{-2}	2.08×10^{-3}	0.00	0.00

In Figure 4, the spectra for the mesh refinements are shown for the microphones at 118° and 90°. The results demonstrate minor differences in band levels between the intermediate and finest meshes, all of which are less than 2 dB, especially for the broadband noise levels

and the first two BPFs. Higher BPF multiples are more evident inn the coarsest mesh, possibly due to resolution effects.



(**a**) Mic at 118° (upstream), $\beta = 0°$ (**b**) Mic at 90°, n = 100

Figure 4. Spectra for mesh refinement.

3.2. Validation

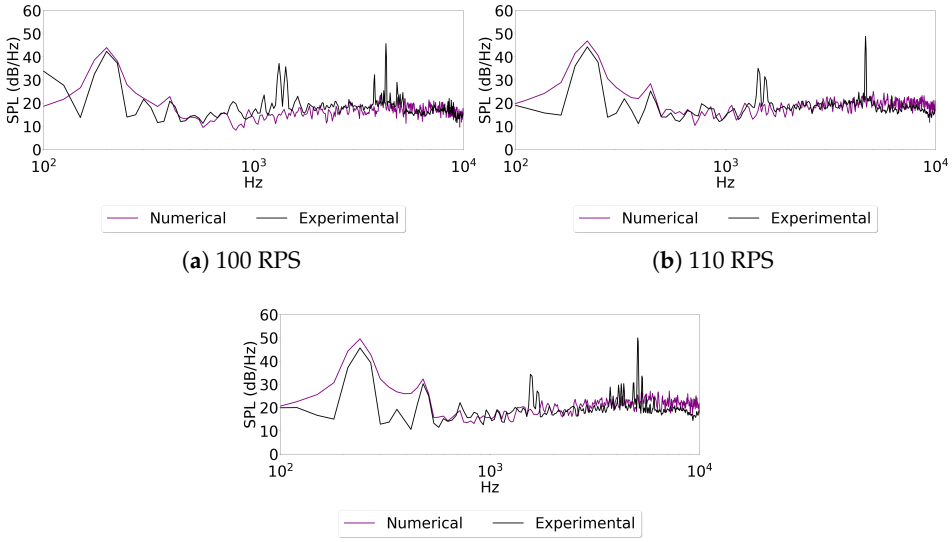
Results for the propeller rotations at three velocities (100, 110, and 120 RPS) for a null pitch increment (Table 2), as well as null advance ratio (no-freestream) are compared against experiments conducted by HKUST [21]. Typically, C_T differences to experiments are below 15%, as the thrust coefficient is stable across all rotations for both experiments and simulations.

Table 2. Comparison of numerical and experimental thrust coefficients at different rotational speeds.

Rotation (RPS)	C_T (Numerical)	C_T (Experimental)	Rel. Error C_T (%)
100	6.25×10^{-2}	7.08×10^{-2}	−11.7
110	6.26×10^{-2}	7.08×10^{-2}	−11.6
120	6.27×10^{-2}	7.29×10^{-2}	−14.0

Numerical and experimental PSD are directly compared in Figure 5 for all the rotations, validating numerical far-field noise calculations. Results are shown for the central microphone (90°). Each figure represents one rotation having a direct comparison between both results. Measurements are only available for a microphone with a 1.5 m radius from the propeller's center, positioned in the propeller's rotation plane.

The experimental and numerical results agree especially in the first BPF (Blade Passing Frequency) level, where differences range between 2 to 5 dB. Deviations are smaller for 100 RPS and increase for 120 RPS. The same behavior occurs for the second BPF. Experimental results contain a peak at 1.5 BPF, which is not present in the numerical simulations, probably occuring due to vibration of the propeller's structural system, which is reported in the literature as Chen et al. [22]. Regarding broadband content, which is dominant in frequencies higher than the second BPF for this propeller, the fidelity of the numerical results is achieved in a margin close to 5 dB across most of the frequencies. Experimental measurements display isolated highly energetic peaks, e.g., the one at 7 kHz. Given the non-physical nature of this peak at low tip Mach numbers (tip Mach below 0.4), it is likely attributable to experimental spurious vibrations or other issues not reported in the experiments. This can be investigated in further studies by conducting a new set of experiments, which is beyond the scope of this manuscript. This validation demonstrates the fidelity of the results to capture general levels and behavior of the first two BPF and broadband noise signatures.



(**a**) 100 RPS (**b**) 110 RPS

(**c**) 120 RPS

Figure 5. Experimental and numerical spectra comparison.

3.3. Aerodynamic Performance Evaluation

An aerodynamic analysis was conducted to quantify the performance of the variable-pitch rotor strategy across a range of operational conditions. The system is evaluated in its ability to maintain thrust and aerodynamic efficiency levels by increasing the collective blade pitch in response to changes in the advance ratio (J) for all the rotations in terms of thrust (C_T), torque coefficients (C_Q) and aerodynamic efficient (η) in Table 3. These points are selected using a low-fidelity Blade Element Momentum Theory (BEMT) method to assess the ability of increasing the collective pitch to prevent a reduction in η as J increases, similar to the procedure in Lattari et al. [23].

Table 3. Performance characteristics of the propeller at different rotations and pitch angles.

Rotation (RPS)	J	β	C_T	C_Q	η
100	0.0	0°	6.25×10^{-2}	6.29×10^{-3}	0.00×10^{0}
100	0.6	5°	2.20×10^{-2}	4.55×10^{-3}	4.61×10^{-1}
100	0.7	10°	3.07×10^{-2}	6.96×10^{-3}	4.92×10^{-1}
100	0.9	15°	2.97×10^{-2}	9.01×10^{-3}	4.71×10^{-1}
110	0.0	0°	6.26×10^{-2}	6.16×10^{-3}	0.00×10^{0}
110	0.6	5°	2.23×10^{-2}	4.49×10^{-3}	4.73×10^{-1}
110	0.7	10°	3.11×10^{-2}	6.90×10^{-3}	5.01×10^{-1}
110	0.9	15°	3.00×10^{-2}	8.95×10^{-3}	4.78×10^{-1}
120	0.0	0°	6.27×10^{-2}	6.11×10^{-3}	0.00×10^{0}
120	0.6	5°	2.25×10^{-2}	4.45×10^{-3}	4.81×10^{-1}
120	0.7	10°	3.21×10^{-2}	6.97×10^{-3}	5.13×10^{-1}
120	0.9	15°	3.00×10^{-2}	8.91×10^{-3}	4.80×10^{-1}

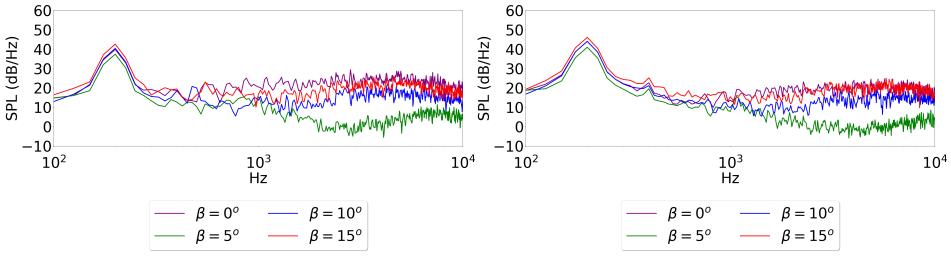
The results demonstrated a consistent thrust level despite increasing advance ratios. For instance, at 120 RPS, the thrust coefficient (C_T) remains stable within the range of 2.25×10^{-2} and 3.21×10^{-2} as the advance ratio J varies from 0.6 to 0.9. However, the increment in pitch is followed by higher torques. Torque coefficient (C_Q) rises significantly for J > 0.6 across all rotational speeds, according to the data. This behavior is a consequence of the larger blade pitch angles, which increase profile drag and thus require greater power input to maintain the target RPS, as it was discussed in the introduction.Thrust and torque balance enables the rotor to operate near constant aerodynamic efficiency (η), preventing

reduction. Even as the torque cost rises at J = 0.9, the efficiency remains stable at a margin, showing only a slight decline. Ultimately, the selected points coupling β and J maintains an aerodynamically favorable configuration, balancing the generation of thrust with the inherent torque penalty.

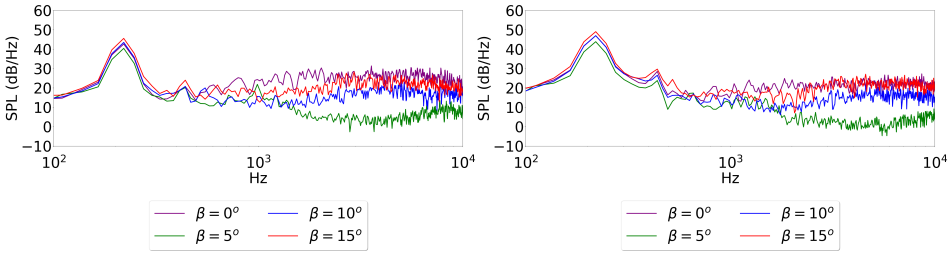
3.4. Noise Levels

Figure 6 present the acoustic spectra characterizing the propeller's noise signature as a function of blade pitch angle (β), rotational speed (n), and observer location. A positive correlation is generally observed between blade pitch angle and noise levels, as tonal noise (spectral peaks at the BPF frequencies) increasing with aerodynamic loading. Comparing the configurations, broadband noise levels are stable within 10 dB, being the $\beta = 0°$ configuration the one presenting the highest broadband levels. However, at $\beta = 5°$, the broadband noise component is almost entirely absent for frequencies above 2 kHz across all rotational speeds, pointing to a reduction in the turbulent flow and vortex mechanisms responsible for high-frequency noise, identifying this pitch setting as an acoustically operating point in terms of broadband noise emission reduction. The next section of the paper investigates this phenomenon by the velocity and vorticity magnitude as well as by the pressure time derivative signature.

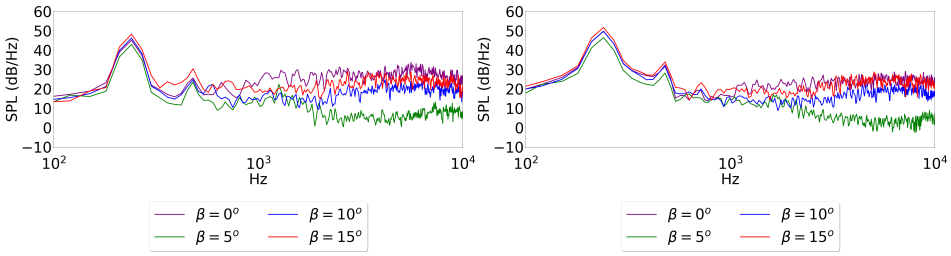
The influence of rotational speed (n) proportionally shifts the BPF harmonics to higher frequencies and elevates the overall SPL of both tonal and broadband. Regarding directivity, the 0-degree central position, registers higher low-frequency broadband noise compared to the 45-degree upstream location.



(**a**) Mic at 118° (upstream), n = 100 (**b**) Mic at 90°, n = 100



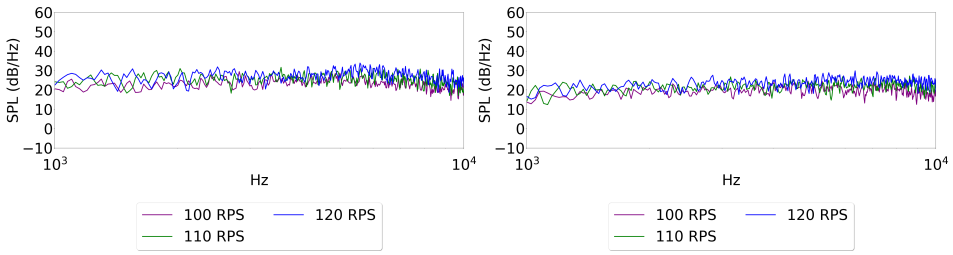
(**c**) Mic at 118° (upstream), n = 110 (**d**) Mic at 90°, n = 110



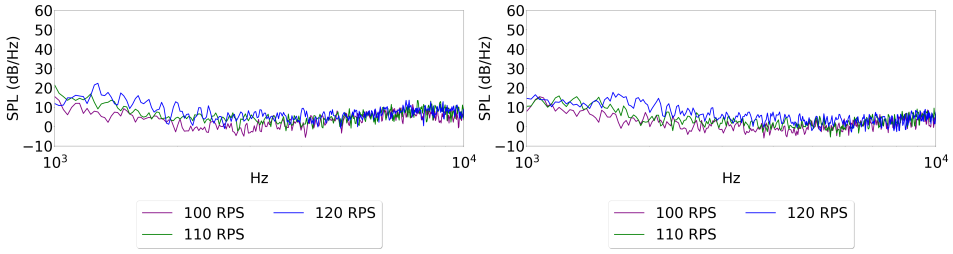
(**e**) Mic at 118° (upstream), n = 120 (**f**) Mic at 90°, n = 120

Figure 6. Numerical pitch effect.

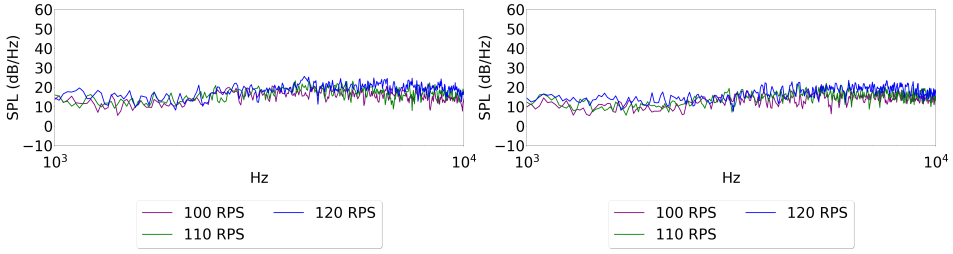
Figure 7 intends to further investigate the broadband level sensitivity, this time focusing on the effect of different rotations. Rotations ranging from 100 to 120 RPS are presented with their respective spectra from 1 kHz to 10 kHz. Each subfigure overlays the rotations with respect to each β value. Results demonstrate that rotational speed has little effect on broadband noise, showing that the collective pitch increment is the dominant effect compared to the rotational speed.



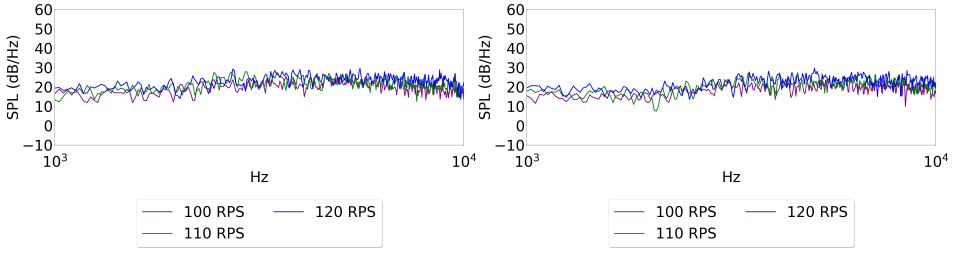
(**a**) Mic at 118° (upstream), $\beta = 0°$ (**b**) Mic at 90°, n = 100



(**c**) Mic at 118° (upstream), $\beta = 5°$ (**d**) Mic at 90°, n = 110



(**e**) Mic at 118° (upstream), $\beta = 10°$ (**f**) Mic at 90°, n = 120



(**g**) Mic at 118° (upstream), $\beta = 15°$ (**h**) Mic at 90°, n = 120

Figure 7. Numerical rotation effect above 1 kHz.

3.5. Flow Field Analysis

Figure 8 presents velocity contours at four radial stations (0.25R, 0.50R, 0.75R, and 0.99R) and four pitch angles (β = 0°, 5°, 10°, and 15°) for a propeller rotational speed of 100 revolutions per second (RPS). Results are collected with the propeller tip aligned with the line of sight to the central microphone, since the propeller phase did not show a significant difference across phases. The remaining propeller rotational speeds are presented in Appendix A, which investigates the effect of the Blade-Vortex Interaction (BVI) on the propeller tips.

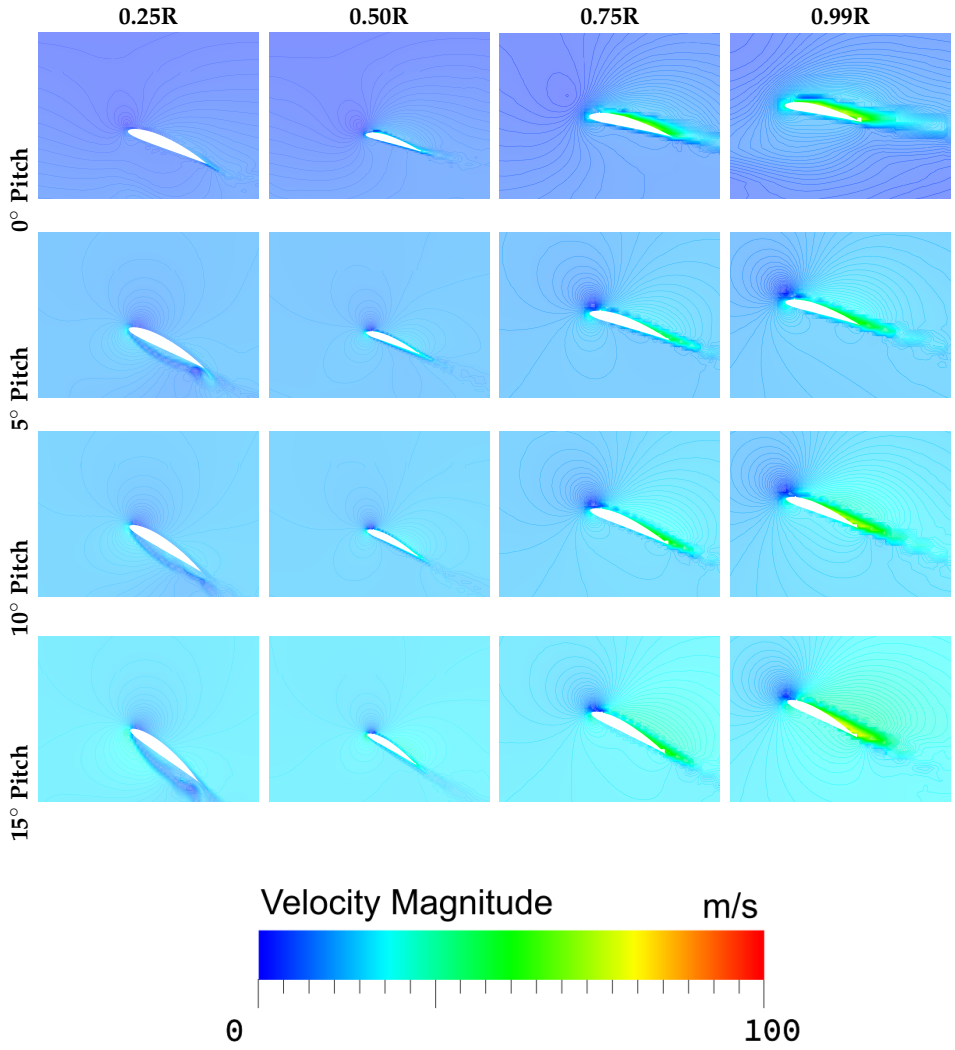


Figure 8. Velocity magnitude distributions across various radial sections (columns) and pitch angles (rows) for the propeller cross-section.

For all the configurations, propeller spanwise velocity gradients radially intensify outboard, as demonstrated when comparing the section at 0.25R to 0.99R, correlating with the increase in linear velocity and radial distance from the hub. As expected for a propeller the velocity differential between the suction and pressure surface is more pronounced at the 0.99R stations. This region is marked by sharp velocity gradients indicating the formation of tip vortex, which appears to be less intense for the lowest collective pitch increment configuration at $\beta = 0°$.

Regarding the collective pitch angle increment with the introduction of a non-null J the blade loading is expected to increase, which deepens the velocity magnitude differences between the suction and pressure surface, mostly concentrated at the propeller trailing edges. As the collective pitch increment is augmented to 5° and 10°, significant flow acceleration over the suction surface is observed, corresponding to an increase in thrust. This effect is limited by flow separation, which becomes evident at $\beta = 15°$. At this condition, a large high velocity region forms on the suction side near the trailing-edge, potentially indicating flow separation, due to the section stall relate to the increment of its angle of attack.

The vorticity magnitude (Figure 9) significantly intensifies outboard due to the higher linear velocity at larger radii. While inboard vorticity (0.25R) remains low and diffuse, the flow strengthens radially, culminating in a highly concentrated core at the tip (0.99R).

This highly concentrated core is identified as the propeller tip vortex, which can lead to Blade Vortex Interaction, a cause for broadband noise [4].

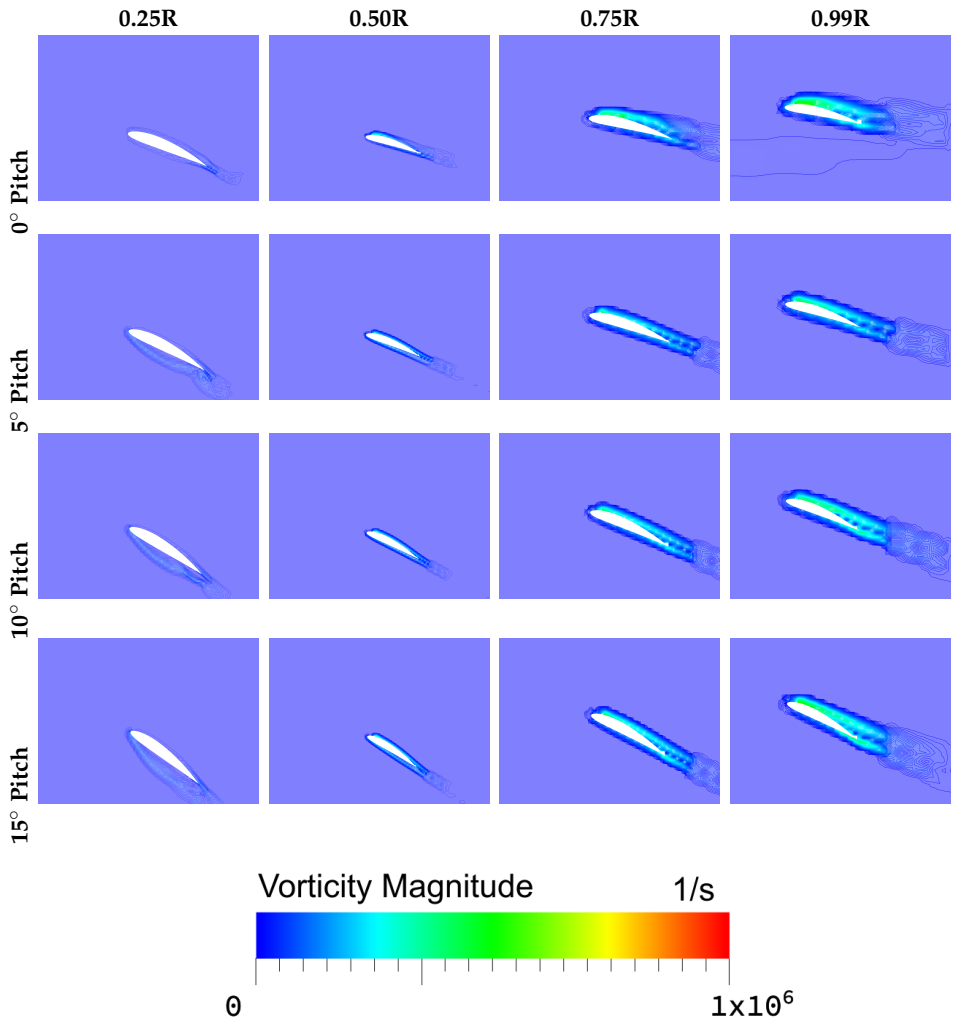


Figure 9. Vorticity magnitude distributions across various radial sections (columns) and pitch angles (rows).

A steady amplification of vorticity is observed across all radial sections as the collective pitch angle increment (β) increases. The $\beta = 0^\circ$ case serves as a baseline, where vorticity is primarily generated by viscous friction. The configuration at $\beta = 5^\circ$ displays a lower vortex magnitude compared to the baseline, an effect that is particularly evident over the suction surface at the 0.75R station. This localized reduction in vorticity provide an explanation for the lower broadband noise levels previously observed for this case. It is important to state that this can happen due to specific characteristics of the tested propeller at this configuration. As β rises, the blade's angle of attack and aerodynamic loading are further incremented, resulting in a larger pressure differential between the pressure and suction surfaces. This increased loading strengthens the shear within the blade's boundary layers and, more significantly, intensifies the cross-flow at the tip, leading to more tip vortex, as evidenced by its increasing magnitude and concentration at 0.99R.

3.6. Pressure Time Derivative Analysis

The pressure time derivative ($\partial p/\partial t$) signatures for all β values at 100 RPS are shown in Figure 10. By quantifying the instantaneous rate of pressure change, this metric serves as an unsteady hydrodynamic forces probe and indicates flow attachment. These unsteady

forces are the direct source mechanisms for loading noise, according to the noise models described in [20]. The figures present the pressure (above) and suction (below) surface for each collective pitch increment at 100 RPS.

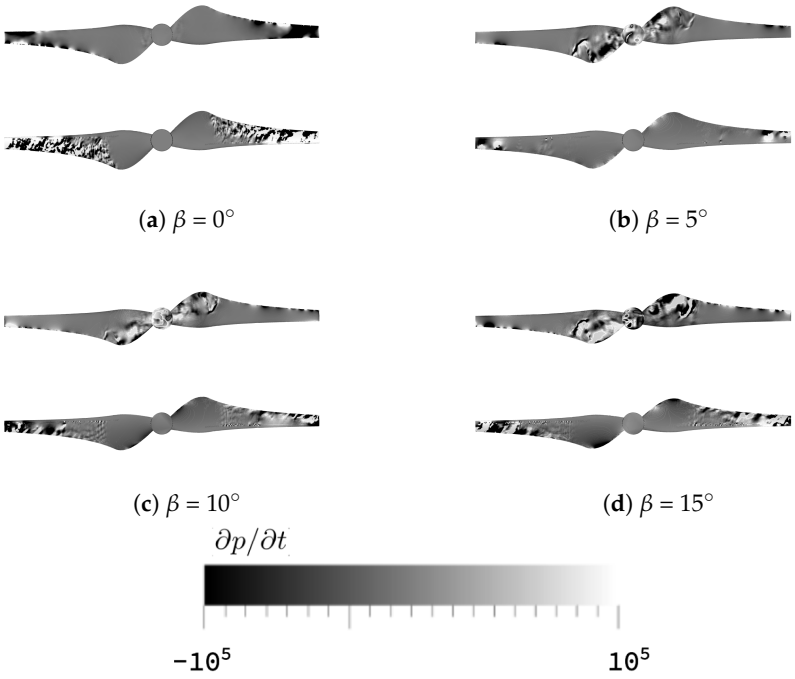


Figure 10. Results for pressure time derivative signature for all the pitch increments.

At the baseline condition ($\beta = 0°$), for the pressure surface, spikes (high magnitudes concentrated in small areas) are observed at the propeller tips, which dissipate for the remaining cases. The inclusion of a non-null advance ratio and consequently positive β also introduces loading complexities in the propeller hub, that deepen as the pitch is incremented. For the pressure surface, the baseline case is the one with a more disturbed pattern; while the remaining cases, with an exception at $\beta = 5°$, present higher magnitudes with spikes. At $\beta = 5°$, pressure time derivative results present lower complexities and spikes compared to the remaing cases, as the patterns retain smooth characteristics. This is more evident for the suction surface, compared to the remaining cases. However, the spikes are concentrated in the blade tips at the trailing edges, which is similar to the other configurations.The behavior can be linked to the suppression of broadband noise observed at $\beta = 5°$, linking this to lower unsteady loads. Considering the results for vortex magnitude, this could be an indication that this configuration was able to contain outboard stall.

As the pitch angle is augmented to $\beta = 10°$ and $15°$, in the suction surface, magnitudes are significantly amplified, and the pressure pulse sharpens, highlighting spikes. This pattern is attributed to the higher angle of attack. These features are symptomatic of unsteady flow phenomena, such as localized flow separation generating unsteady loading and, consequently, broadband noise content. Combining this finding with the increase in vorticity outboard, it is possible to discern an unattached flow phenomenon leading to localized propeller stall outboard. In contrast, the $\beta = 5°$ maintains a largely attached flow, thereby mitigating the outboard propeller stall that becomes evident at higher pitch angles.

4. Conclusions

This study numerically investigated the aerodynamic and aeroacoustic performance of a dual-bladed, 240 mm variable-pitch propeller, motivated by the need to optimise performance and noise signatures for next-generation electric aircraft, such as eVTOLs and drones. The ability of electric motors to provide high torque at lower rotational speeds allowed propellers to operate with higher pitch angles in response to increasing forward flight velocities, presenting a balance between noise levels and aerodynamic performance. A numerical parametric study, using three collective pitch variations at rotations ranging from 100 to 120 RPS, demonstrated satisfactory validation against experimental results. Predicted thrust showed discrepancies within 15% of experimental values, while Blade Passage Frequency (BPF) levels were accurately matched within a 2–5 dB margin. Broadband noise predictions were also captured, generally remaining within a 5 dB margin of the experimental data.

Increasing the collective pitch angle in response to a higher advance ratio (forward flight condition) prevents aerodynamic efficiency and thrust levels reductions, however at the cost of higher required torque. Spectral analysis confirms that the pitch increment generally introduces additional tonal noise, however broadband noise is generally maintained in a 10 dB, comparing to the baseline case (null pitch increment). Conversely to this pattern, the $+5^{\circ}$ collective pitch in response to an advance factor ratio of 0.6, which suppressed broadband noise at frequencies above 2 kHz. This configuration was shown to mitigate outboard stall, reducing strong tip vortex formation and propeller suction-side unsteady loading, according to flow field analysis (velocity and vorticity magnitude) and pressure time derivative analysis on its surface pressure signature.

This work was able to demonstrate the feasibility of a numerical parametric study for exploring the collective pitch angle increment in response to higher advance ratios, demonstrating a fair validation against experimental data as well as exploring the unsteady loading dynamic of the configurations.

Author Contributions: Conceptualization, M.G.L., V.H.P.d.R., F.D.d.S. and C.J.D.; Methodology, M.G.L. and C.J.D.; Software, M.G.L. and C.J.D.; Validation, M.G.L. and F.D.d.S.; Formal analysis, M.G.L.; Investigation, M.G.L. and C.J.D.; Resources, C.J.D.; Writing—original draft, M.G.L.; Writing—review & editing, C.J.D.; Visualization, M.G.L.; Funding acquisition, C.J.D. All authors have read and agreed to the published version of the manuscript.

Funding: This research received no external funding.

Institutional Review Board Statement: Not applicable.

Informed Consent Statement: Not applicable.

Data Availability Statement: The data presented in this study are available on request from the corresponding author.

Conflicts of Interest: The funders had no role in the design of the study; in the collection, analyses, or interpretation of data; in the writing of the manuscript; or in the decision to publish the results.

Nomenclature

Symbol	Description
f_i	Probability density function
$\mathbf{x}$	Position vector
c_i	Discrete lattice velocity
Δt	Time step

$C(\mathbf{x}, t)$	Molecular collision term
k	Turbulent kinetic energy
$\vec{u}$	Velocity vector
P_k	Production of turbulent kinetic energy
$C_{\epsilon 1, \epsilon 2, \mu}$	Turbulence model constants
S_{xx}	Auto-spectral density
T	Thrust force
Q	Torque
n	Rotational speed (rev/s)
D	Propeller diameter
J	Advance ratio (V/nD)
V	Freestream velocity
C_t	Thrust coefficient
C_q	Torque coefficient
r	Propeller Radial Position
R_{tip}	Propeller tip radius
c/R_{tip}	Propeller chord distribution
θ	Propeller twist angle
dZ_C/R_{tip}	Propeller camber distribution
dZ_C	Propeller camber height
ϵ	Turbulent dissipation rate
ν	Kinematic viscosity
ν_T	Turbulent (eddy) viscosity
$\sigma_k, \sigma_\epsilon$	Turbulent Prandtl numbers for k and ϵ
ρ	Fluid density
Δf_b	Frequency bandwidth
η	Propeller aerodynamic efficiency
β	Collective pitch angle increment

Appendix A

In Figures A1 and A2, velocity and vorticity magnitudes are analyzed across different rotational speeds. Each figure presents results at the 0.99R section with respect to the propeller span for each rotation and each collective pitch setting. The main objective is to analyze the effects on the flow field, particularly those related to Blade-Vortex Interaction (BVI) across different rotations. Results demonstrate that β is the dominant effect (different rows in the figure), whereas the rotational speed appears to only intensify the velocity levels but not the overall pattern of the velocity contour. A similar effect can be discerned for the vorticity magnitude, providing evidence that BVI is not a dominant factor for this particular propeller, regardless of the increment in the advance ratio coupled with higher β values, as there is no evidence of high-level vorticity in the propeller tips as a effect of higher rotational speed.

https://doi.org/10.3390/fluids11020031

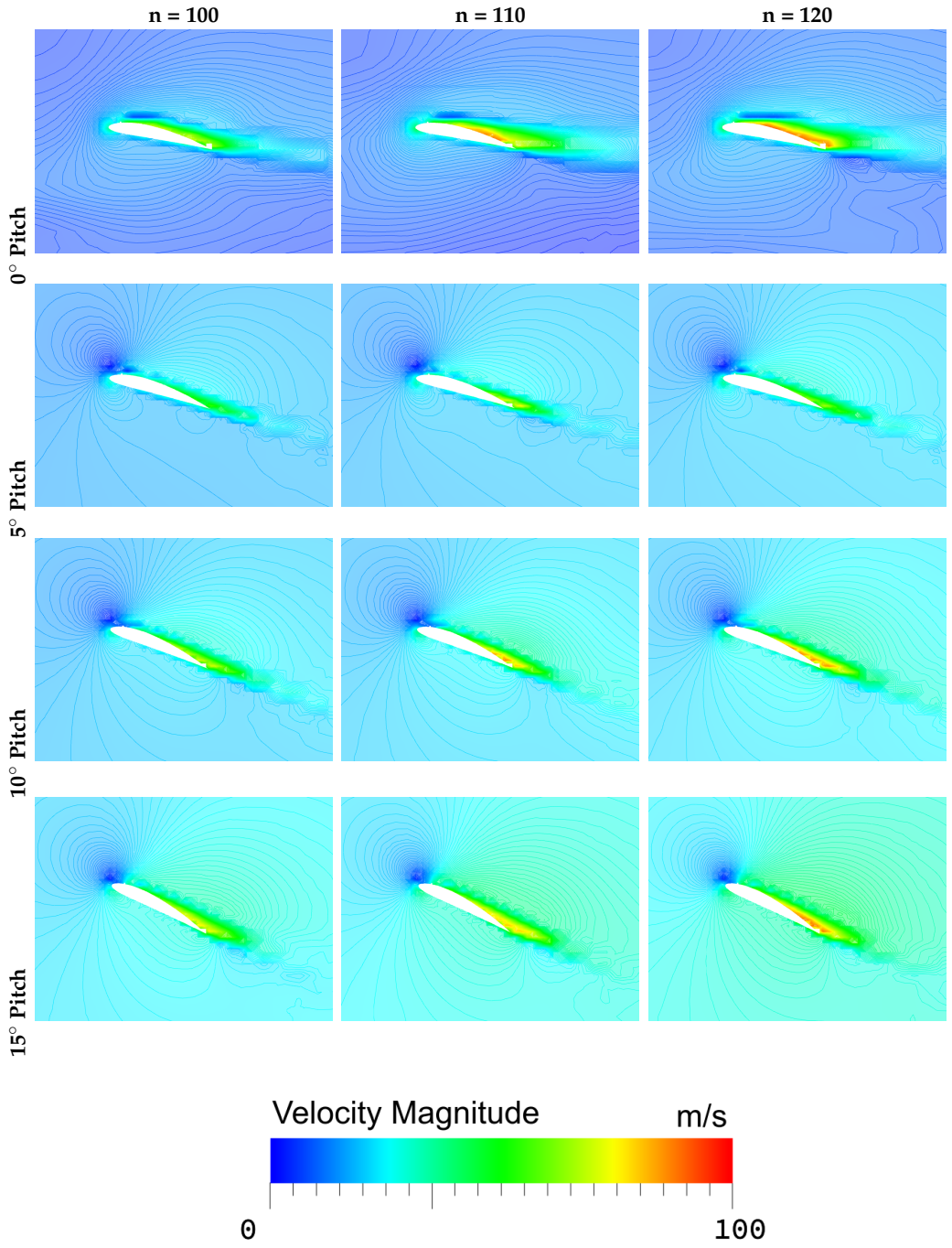


Figure A1. Velocity magnitude distributions at the 0.99R radial section for different rotational speeds (columns) across pitch angles (rows).

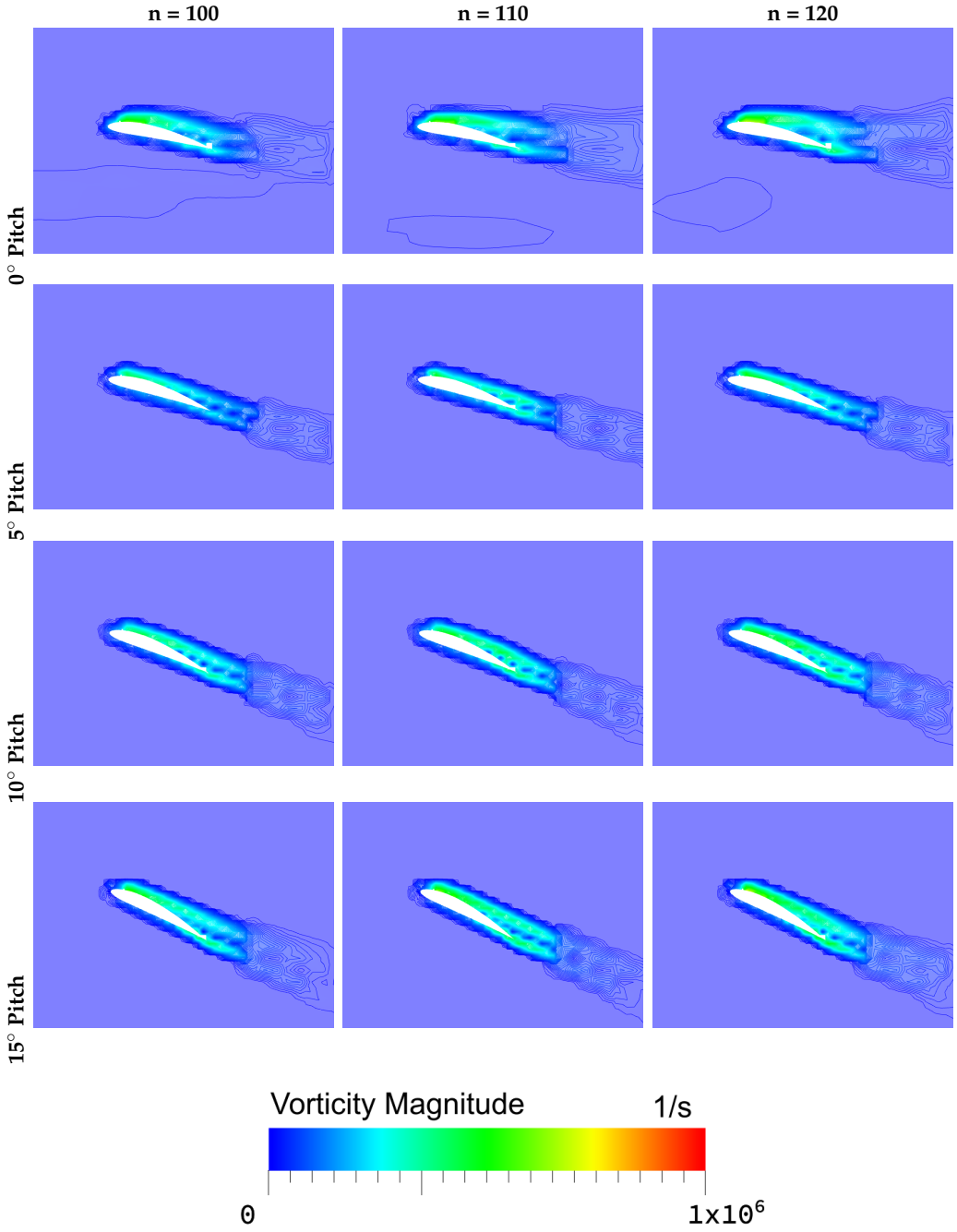


Figure A2. Vorticity magnitude distributions at the 0.99R radial section for different rotational speeds (columns) across pitch angles (rows).

References

1. Takahashi, K.; Fujimoto, H.; Hori, Y.; Kobayashi, H.; Nishizawa, A. Modeling of propeller electric airplane and thrust control using advantage of electric motor. In Proceedings of the 2014 IEEE 13th International Workshop on Advanced Motion Control (AMC), Yokohma-city, Japan, 14–16 March 2014; pp. 482–487. [CrossRef]
2. Rohacs, J.; Rohacs, D. Conceptual design method adapted to electric/hybrid aircraft developments. *Int. J. Sustain. Aviat.* **2019**, *5*, 175–189. [CrossRef]
3. ICAO. *ICAO ANNEX 16: Environmental Protection*; ICAO: Montreal, QC, Canada, 2017.
4. Marte, J.; Kurtz, D. *A Review of Aerodynamic Noise from Propellers, Rotors, and Lift Fans*; JPL Technical Report; Jet Propulsion Laboratory, California Institute of Technology: Pasadena, CA, USA, 1970.
5. Yang, Y.; Liu, Y.; Li, Y.; Arcondoulis, E.; Wang, Y.; Li, W.; Huang, B. Aerodynamic and Aeroacoustic characteristics of a multicopter propeller during forward flight. In Proceedings of the 2018 Joint Propulsion Conference, Cincinnati, OH, USA, 9–11 July 2018. [CrossRef]

6. Sadraey, M. *Aircraft Performance: An Engineering Approach*; CRC Press: Boca Raton, FL, USA, 2017.
7. Zawodny, N.S.; Boyd, D.D., Jr.; Burley, C.L. Acoustic characterization and prediction of representative, small-scale rotary-wing unmanned aircraft system components. In *American Helicopter Society (AHS) Annual Forum*; American Helicopter Society (AHS): Fairfax, VA, USA, 2016.
8. Berton, J.J.; Nark, D.M. Low-noise operating mode for propeller-driven electric airplanes. *J. Aircr.* **2019**, *56*, 1708–1714. [CrossRef]
9. Podsędkowski, M.; Konopiński, R.; Obidowski, D.; Koter, K. Variable Pitch Propeller for UAV-Experimental Tests. *Energies* **2020**, *13*, 5264. [CrossRef]
10. Podsędkowski, M.; Konopiński, R.; Lipian, M. Acoustic Stall Detection of Variable Pitch Propeller for Unmanned Aerial Vehicles. *J. Intell. Robot. Syst.* **2023**, *109*, 70. [CrossRef]
11. Huang, G.; Sharma, A.; Chen, X.; Riaz, A.; Jefferson-Loveday, R. Numerical Predictions of Low-Reynolds-Number Propeller Aeroacoustics: Comparison of Methods at Different Fidelity Levels. *Aerospace* **2025**, *12*, 154. [CrossRef]
12. Liu, X.; Zhao, H.; Li, Z.; Ai, H.; Chen, Z.; Dai, Y. Research on Variable Pitch Propeller Control Technology of eVTOL Based on ADRC. *Electronics* **2025**, *14*, 3627. [CrossRef]
13. Yu, K.; Ko, J.; Jeong, J.; Lee, S. Comparative analysis of fixed-pitch and variable-pitch control systems for multirotor drones: Acoustic characteristics and rotor phase control. *J. Sound Vib.* **2024**, *573*, 118187. [CrossRef]
14. SIMULIA PowerFLOW Userguide, 2019. Available online: https://dam.technia.com/cdn/5FPHbsF/dassault-systemes-simulia-powerflow-datasheet.pdf (accessed on 11 December 2025).
15. Gonzalez-Martino, I.; Wang, J.; Romani, G.; Casalino, D. Rotor noise generation in a turbulent wake using the lattice-boltzmann method. In Proceedings of the 2018 AIAA/CEAS Aeroacoustics Conference, Atlanta, Georgia, 25–29 June 2018. [CrossRef]
16. Avallone, F.; van der Velden, W.; Ragni, D.; Casalino, D. Noise reduction mechanisms of sawtooth and combed-sawtooth trailing-edge serrations. *J. Fluid Mech.* **2018**, *848*, 560–591. [CrossRef]
17. Avallone, F.; van den Ende, L.; Li, Q.; Ragni, D.; Casalino, D.; Eitelberg, G.; Veldhuis, L. Aerodynamic and Aeroacoustic Effects of Swirl Recovery Vanes Length. *J. Aircr.* **2019**, *56*, 2223–2235. [CrossRef]
18. Casalino, D.; Grande, E.; Romani, G.; Ragni, D.; Avallone, F. Definition of a benchmark for low Reynolds number propeller aeroacoustics. *Aerosp. Sci. Technol.* **2021**, *113*, 106707. [CrossRef]
19. Zhu, T.; Carolus, T.H. Axial fan tip clearance noise: Experiments, Lattice–Boltzmann simulation, and mitigation measures. *Int. J. Aeroacoust.* **2018**, *17*, 159–183. [CrossRef]
20. Brès, G.; Pérot, F.; Freed, D. A Ffowcs Williams—Hawkings Solver for Lattice-Boltzmann Based Computational Aeroacoustics. In Proceedings of the 16th AIAA/CEAS Aeroacoustics Conference, Stockholm, Sweden, 7–9 June 2010. [CrossRef]
21. HKUST. *Configuration of the Study of Isolated Motor*; HKUST: Hong Kong, China, 2020.
22. Chen, W.; Ma, Z.; Spieser, E.; Guo, J.; Zhou, P.; Zhong, S.; Zhang, X.; Huang, X. Acoustic imaging of the broadband noise arising in contra-rotating co-axial propellers. *Aerosp. Sci. Technol.* **2023**, *141*, 108531. [CrossRef]
23. Lattari, M.G.; Rosa, V.H.; Deschamps, C.J. Numerical Analysis of Aerodynamics and Acoustics of a Variable Pitch Propeller. In Proceedings of the AIAA AVIATION 2023 Forum, San Diego, CA, USA and Online, 12–16 June 2023. [CrossRef]

Disclaimer/Publisher's Note: The statements, opinions and data contained in all publications are solely those of the individual author(s) and contributor(s) and not of MDPI and/or the editor(s). MDPI and/or the editor(s) disclaim responsibility for any injury to people or property resulting from any ideas, methods, instructions or products referred to in the content.